

Dynamical coupled-channels approach to electroweak meson productions on nucleon and deuteron

Satoshi X. Nakamura^{1,2,a)}

¹University of Science and Technology of China, Hefei 230026, People's Republic of China

²State Key Laboratory of Particle Detection and Electronics (IHEP-USTC), Hefei 230036, People's Republic of China

^{a)}Corresponding author: satoshi@ustc.edu.cn

Abstract. I overview our recent activity with the Argonne-Osaka dynamical coupled-channels (DCC) approach that provides a unified description of various electroweak meson productions on single nucleon and nucleus. First I discuss the DCC model of a single nucleon. The DCC model has been developed through a comprehensive analysis of $\pi N, \gamma N \rightarrow \pi N, \eta N, K\Lambda, K\Sigma$ reaction data. The model has been further extended to finite Q^2 region by analyzing pion electroproduction data, and to neutrino-induced reactions using the PCAC relation. Next I discuss applications of the DCC model to electroweak meson productions on the deuteron. We consider impulse mechanism supplemented by final state interactions (FSI) due to NN and meson-nucleon rescatterings. Using this model, I discuss FSI corrections needed to extract γ -neutron reaction observables from $\gamma d \rightarrow \pi NN$, and a novel method to extract ηN scattering length from $\gamma d \rightarrow \eta pn$. I also discuss FSI corrections on the existing neutrino-nucleon pion production data that had been extracted from neutrino-deuteron data.

Introduction

Electroweak meson productions on nucleon and deuteron have been attracting physicists' interests. This is primarily because the reactions are very useful for studying the baryon spectroscopy. By analyzing data of these processes, we can identify nucleon resonances and extract their properties such as mass, width, and electromagnetic form factors. Combining these properties with outputs from hadron structure models and Lattice QCD, we can better understand QCD in the nonperturbative regime. Our another interest in the processes is to obtain a basis to study electroweak meson productions on nuclei. Using the obtained single nucleon amplitudes as a basis, we can address medium modifications on the propagations of mesons and nucleon resonances in nuclear matter. We can also study neutrino-nucleus reactions, understanding of which is highly demanded for extracting the neutrino properties from ongoing neutrino oscillation experiments.

The Argonne(ANL)-Osaka Collaboration [1] has proved a dynamical coupled-channels (DCC) approach very successful in describing electroweak meson productions on nucleon and deuteron, and in extracting nucleon resonance properties. While other common framework such as the K-matrix model [2] has been also successful in this regard, a unique feature in the DCC approach is that it provides reaction mechanisms and dynamical contents of the nucleon resonances in terms of hadronic degrees of freedom. Also, the DCC model for meson-baryon reactions is compatible well with multiple scattering theory for many-body system, and thus applications of amplitudes from the DCC model to nuclear processes can be done straightforwardly (not necessarily easy though) without introducing artificial prescriptions.

This contribution is about reviewing our recent activity with the DCC approach. The former part is on the DCC approach to the single nucleon sector. First we discuss the DCC analysis of $\pi N, \gamma N \rightarrow \pi N, \pi\pi N, \eta N, K\Lambda, K\Sigma$ reactions. Then the DCC model is extended to finite Q^2 region and neutrino-induced meson productions. The latter part is about applications of the DCC model to electroweak meson productions on the deuteron. Specifically we discuss three subjects. The first one is about extracting neutron-target observables from $\gamma d \rightarrow \pi NN$. The second one is about a novel method of extracting η -nucleon scattering length from $\gamma d \rightarrow \eta np$. The last one is on FSI corrections to neutrino-nucleon cross section data from neutrino-deuteron experiments.

Dynamical coupled-channels approach to $\pi N, \gamma N \rightarrow \pi N, \pi\pi N, \eta N, K\Lambda, K\Sigma$

The dynamical coupled-channels model is designed to describe electroweak meson productions off the nucleon in the resonance region ($W \lesssim 2$ GeV). It is based on a coupled-channel Lippmann-Schwinger equation that takes care of couplings among $\pi N, \pi\pi N, \eta N, K\Lambda, K\Sigma, \pi\Delta, \rho N, \sigma N$ channels to satisfy the unitarity. The electroweak couplings are considered perturbatively. The meson-baryon interactions in the model consist of non-resonant meson-exchange mechanisms and resonant bare N^* -excitation mechanisms. By solving the Lippmann-Schwinger equation, the bare N^* states are dressed by meson clouds to form nucleon resonances. The DCC model has been developed through a comprehensive analysis of $\pi N, \gamma N \rightarrow \pi N, \eta N, K\Lambda, K\Sigma$ reaction data; the number of data points amounts to be $\sim 27,000$. The quality of fitting the data achieved with the DCC model can be found in Refs. [3, 4]. The parameters associated with the nucleon resonances such as pole positions and helicity amplitudes have been successfully extracted from the DCC model amplitudes [3, 4]. All ANL-Osaka DCC analysis results and partial wave amplitudes are collected in Ref. [1].

Extension of the DCC model to finite Q^2 region and neutrino reactions

Ongoing and near-future neutrino oscillation experiments such as T2K [5] and DUNE [6] primarily aim at discovering the CP violation in the lepton sector and determining the neutrino mass hierarchy. They need a high-precision neutrino-nucleus pion production model for this purpose, because neutrino-nucleus reactions they utilize to detect neutrinos cover the whole resonance region ($W \lesssim 2$ GeV) and higher W region. An essential ingredient to develop a neutrino-nucleus reaction model is an elementary neutrino-nucleon reaction model, and we will develop one by extending the DCC model.

First we need to extend the vector current, which has been determined by analyzing the photo-reaction data, to finite Q^2 region. This amounts to determine the Q^2 -dependence of the vector $N \rightarrow N^*$ transition form factors. This can be done by analyzing a good amount of available data for electron-induced reactions on the nucleon, including both single pion productions and inclusive processes. We analyze both proton- and neutron-target data because, once the analysis is completed, we need to separate the vector current into the isovector and isoscalar parts; the isovector current is necessary to describe charged-current reactions. An analysis result for the inclusive electron-proton scattering is shown in Fig. 1. The quality of the fit is reasonable enough for an application to the neutrino reactions. The two-pion productions give a sizable contribution in the higher W region, as shown by the difference between the red solid and magenta dashed curves.

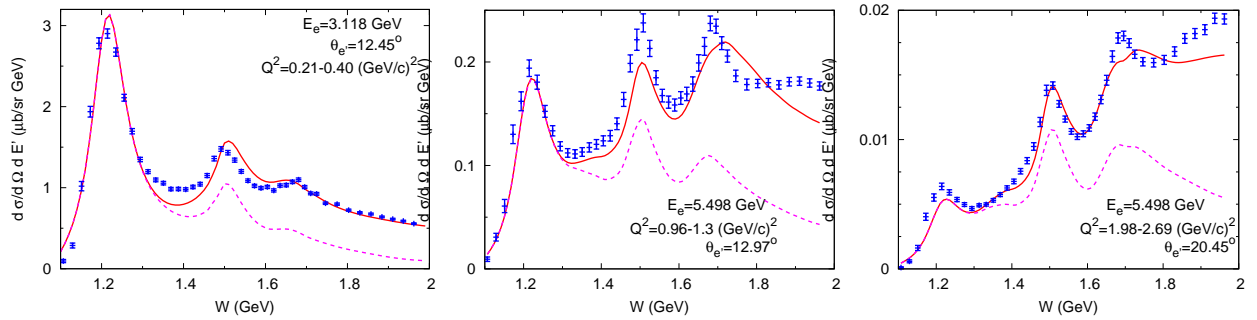


FIGURE 1. Differential cross sections for inclusive electron-proton scattering from the DCC model. The red solid (magenta dashed) curves are for inclusive cross sections (contributions from the πN final states). The data are from Ref. [7].

Regarding the axial current, we have to take a different strategy because we have scarce neutrino data available, except for some useful data for the $\Delta(1232)$ region only. Thus we follow a guiding principle to derive the axial current: the PCAC relation with the πN reaction amplitudes. Using the relation, we can relate the axial $N \rightarrow N^*$ transition form factors ($g_{AN \rightarrow N^*}$) at $Q^2 \sim 0$ to the $\pi N \rightarrow N^*$ coupling strengths ($g_{\pi N \rightarrow N^*}$) as $g_{AN \rightarrow N^*}(Q^2 \sim 0) \simeq g_{\pi N \rightarrow N^*}$; the phases of the form factors are also fixed. This can be done only when both πN amplitudes and axial currents are developed consistently with the PCAC relation. So far, only the DCC model has achieved this [8]. On the other hand, what has been commonly done is to take $N^* \rightarrow \pi N$ decay width (from the PDG) and therefore $|g_{\pi N \rightarrow N^*}|$, and use the

relation $g_{AN \rightarrow N^*}(Q^2 \sim 0) \simeq |g_{\pi N \rightarrow N^*}|$. Obviously, the phase cannot be determined in a controllable manner. Regarding the Q^2 -dependence, we still need an assumption because of lack of the data. A conventional choice is to use a dipole form factor with the cutoff of ~ 1 GeV.

With the model setup described above, we make a prediction for total cross sections of neutrino-nucleon reactions, as shown in Fig. 2. The DCC model prediction is consistent with the BNL data. The model still has a flexibility to adjust the axial $N \rightarrow N^*$ form factors to fit the ANL data. The DCC model is currently only available neutrino-induced two pion production model covering the whole resonance region. The amplitudes from the DCC model are being implemented into ongoing and forthcoming neutrino oscillation experimental analyses.

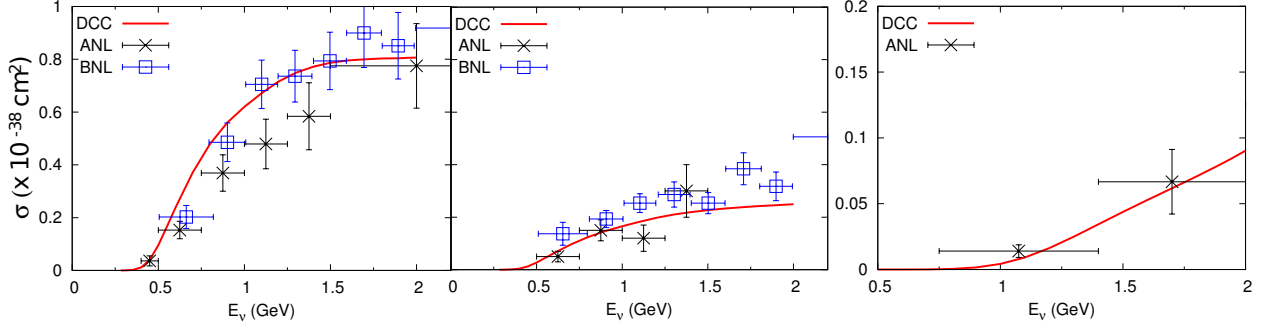


FIGURE 2. Total cross sections for neutrino-nucleon pion productions from the DCC model. (left) $\nu_\mu p \rightarrow \mu^- \pi^+ p$; (center) $\nu_\mu n \rightarrow \mu^- \pi^+ p$; ANL (BNL) data are from Ref. [9] ([10]). (right) $\nu_\mu p \rightarrow \mu^- \pi^+ \pi^0 p$ and the data are from Ref. [11]. Figures taken from Ref. [8]. Copyright (2015) APS.

Application of the DCC model to electroweak meson productions on deuteron

Our model for electroweak meson productions on the deuteron is based on the multiple scattering theory truncated at the first order rescattering. Therefore our deuteron reaction model consists of the impulse, NN rescattering, and meson-nucleon rescattering mechanisms, as depicted in Fig. 3. The diagrams are built with elementary (off-shell) amplitudes such as the vector and axial currents and meson-baryon scattering amplitudes from the DCC model. Also, the model includes the NN scattering amplitudes and the deuteron wave function for which we employ the CD-Bonn potential [12].

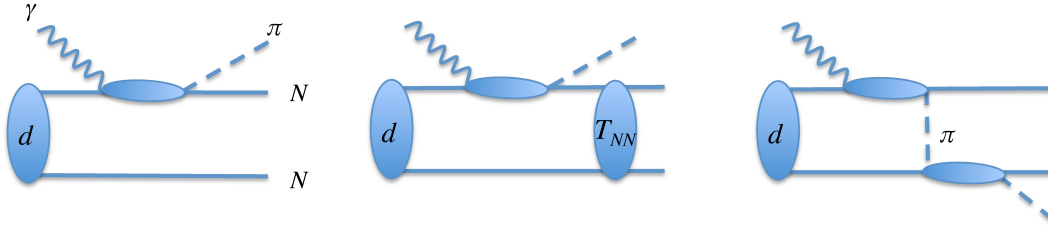


FIGURE 3. The $\gamma d \rightarrow \pi NN$ model in this work. (left) impulse, (center) NN rescattering, (right) πN rescattering mechanisms.

Using the model described above, we can make a parameter-free prediction for meson photoproduction off the deuteron as shown in Fig. 4. The black dotted curves in the figures are obtained by including the impulse mechanism only. As seen in Fig. 4(a), $\gamma d \rightarrow \pi^0 pn$ cross sections from the impulse approximation significantly overshoot the data. However, the final state interactions (FSI) bring the calculation into a good agreement with the data. This large FSI effect is due to the orthogonality of the NN scattering wave function and the deuteron wave function. On the other hand, the FSI effect is very small for $\gamma d \rightarrow \pi^- pp$ as seen in Fig. 4(b). Regarding $\gamma d \rightarrow \eta pn$ as shown in Fig. 4(c), the FSI effect does not seem very large, except for the backward η production where a significant enhancement due to $\eta N \rightarrow \eta N$ brings the calculation into an excellent agreement with the data. In what follows, we will study three interesting problems using this DCC-based deuteron reaction model.

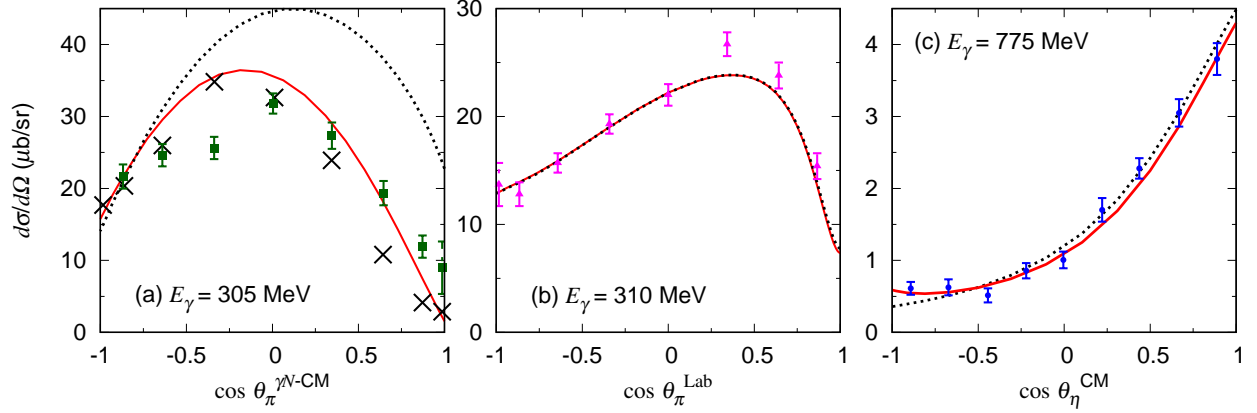


FIGURE 4. Differential cross sections for meson photoproductions off the deuteron. (a) $\gamma d \rightarrow \pi^0 pn$, (b) $\gamma d \rightarrow \pi^- pp$, and (c) $\gamma d \rightarrow \eta pn$. The black dotted curves are calculated with the impulse mechanism only, while the red solid curves are from the full model including also the NN and meson-nucleon rescattering mechanisms. Data are from Refs. [13] (green squares), [14] (black crosses), [15] (magenta triangles), and [16] (blue circles). Figures (a,b) taken from Ref. [17] and figure (c) from Ref. [18]. Copyright (2017) APS.

Extraction of neutron-target observables from $\gamma d \rightarrow \pi NN$

Data for pion photoproduction off the proton and neutron constitute a base for studying the baryon spectroscopy. Because of unavailability of the free neutron target, the deuteron is the primary target to measure the neutron-target observables, and we need to understand how to extract it from the deuteron-target data. Commonly, one extracts the γ - n cross sections by applying a certain set of kinematical cuts, assuming that the selected events are from single-nucleon quasi-free processes. However, a concern remains whether FSI effects and/or the kinematical cuts could distort the extracted observables from the free ones. We will address this question.

Our procedure is as follows. Starting with the DCC $\gamma N \rightarrow \pi N$ amplitudes, we implement them in the deuteron reaction model and calculate deuteron-target cross sections to which kinematical cuts are applied. Using the extraction formula given in Ref. [19], the neutron-target observables are obtained. Then the extracted observables are compared with the corresponding free ones directly calculated from the DCC $\gamma n \rightarrow \pi n$ amplitudes. In this analysis, we use realistic kinematical cuts used in recent JLab analyses [20, 21, 22]. In addition, we also consider a cut on W from the final pion-nucleon kinematics, as has been done in the MAMI analysis [23, 24]. In the JLab analyses [20, 21, 22], on the other hand, W is inferred assuming the kinematics where the initial neutron is at rest. We critically examine the validity of this assumption.

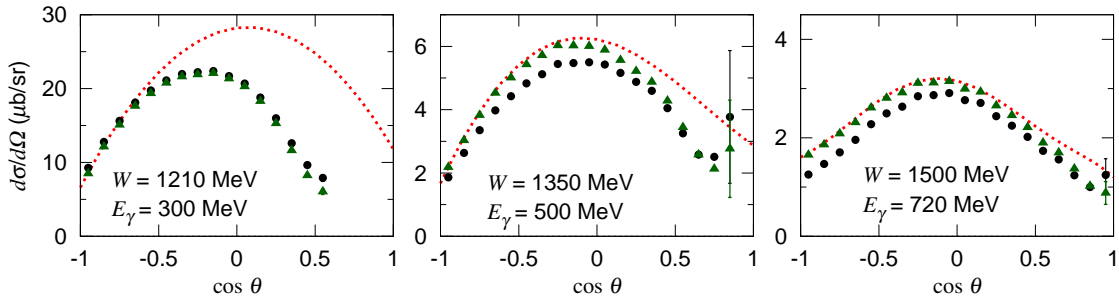


FIGURE 5. Pion angular distribution for $\gamma n \rightarrow \pi^0 n$. The black circles (green triangles) are extracted from $\gamma d \rightarrow \pi^0 pn$ generated by the DCC-based model including the impulse + NN -rescattering + πN -rescattering (impulse + NN -rescattering) terms. The W -cut is considered in the extraction. The red dotted curves are the free $\gamma n \rightarrow \pi^0 n$ cross sections at W from the ANL-Osaka model. Figures taken from Ref. [19]. Copyright (2018) APS.

The $\gamma n \rightarrow \pi^0 n$ differential cross sections extracted from $\gamma d \rightarrow \pi^0 p n$ are shown in Fig. 5. The NN -rescattering largely reduce the cross sections at $E_\gamma = 300$ MeV. Meanwhile, the πN -rescattering effect is negligibly small at $E_\gamma = 300$ MeV, as indicated by the small differences between the black circles and green triangles. As the photon energy increases, however, the πN -rescattering becomes comparable to the NN -rescattering, and significantly reduces the cross sections overall except the forward pion angles. Clearly, the kinematical cuts cannot remove the FSI effects, and thus FSI corrections are necessary. Also, the FSI effects seen in Fig. 5 are qualitatively very similar to, and thus the first theoretical explanation of, those found in the MAMI analysis [23, 24].

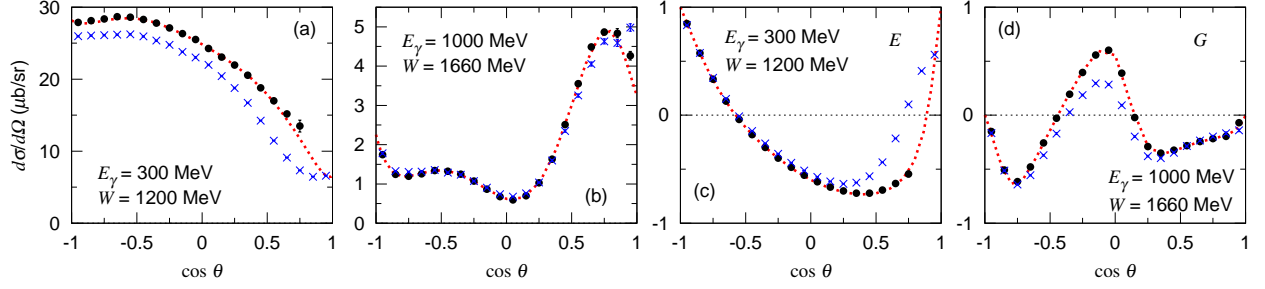


FIGURE 6. (a,b) Unpolarized differential cross sections for $\gamma n \rightarrow \pi^- p$ extracted from $\gamma d \rightarrow \pi^- p p$ generated from the DCC-based model including only the quasi-free mechanism. The black circles [blue crosses] are extracted with [without] W cut. (c)[(d)] The polarization observables E [G] for $\gamma n \rightarrow \pi^- p$ extracted from $\gamma d \rightarrow \pi^- p p$. The other features are the same as those in Fig. 5. Figures taken from Ref. [19]. Copyright (2018) APS.

Now we examine the extraction without the W -cut as employed in the recent JLab analyses. For this study, we do not consider the FSI. The $\gamma n \rightarrow \pi^- p$ observables including the polarization observables of E and G are shown in Fig. 6. With the W -cut, the extracted observables (black circles) accurately reproduce the free ones (red dotted curves). Without the W -cut, however, the extracted observables (blue crosses) sometimes significantly deviate from the free ones. This deviation is caused by the Fermi motion. The result indicates that it is important to apply the W -cut to suppress the problematic Fermi motion effect, thereby extracting the neutron-target observables accurately.

Low-energy η -nucleon interaction studied with $\gamma d \rightarrow \eta n p$

The η -nucleon scattering length ($a_{\eta N}$) governs the low-energy behavior of the η -nucleon scattering which is a basic feature of the meson-baryon dynamics. Also, the existence of exotic η -mesic nuclei strongly depends on its value [25]. Being the important quantity, however, $a_{\eta N}$ has not been well determined yet. Several coupled-channel analyses have been done on the $\pi N \rightarrow \pi N, \eta N$ and $\gamma N \rightarrow \pi N, \eta N$ reaction data to determine $a_{\eta N}$. The $p n \rightarrow \eta d$ reaction has also been analyzed. The imaginary part of $a_{\eta N}$ from these analyses is fairly consistent, falling into $\text{Im}[a_{\eta N}] = 0.2\text{--}0.3$ fm. However, the real part is in a significantly wider range of $\text{Re}[a_{\eta N}] = 0.2\text{--}0.9$ fm [25]. Because $a_{\eta N}$ has been extracted from the indirect information, the model dependence is difficult to avoid. To better determine $a_{\eta N}$, we need a process that sensitively probes the $\eta N \rightarrow \eta N$ scattering, while the other background mechanisms being suppressed.

A realization of this idea is the ongoing experiment at the Research Center for Electron Photon Science (ELPH), Tohoku University [26]. In this experiment, the $\gamma d \rightarrow \eta n p$ cross section is measured at a special kinematics: $E_\gamma \sim 0.94$ GeV and $\theta_p \sim 0^\circ$ (θ_p : angle between the scattered proton and the incident photon). At this kinematics, the produced η is almost at rest and very likely to interact with the spectator neutron. The scattered proton with a large momentum has little chance to interact with the η and neutron. We refer to this special kinematics as the ELPH kinematics. The ELPH kinematics seems ideal to study the low-energy η -nucleon interaction. A model is still necessary to extract $a_{\eta N}$ from the ELPH data, and the DCC-based $\gamma d \rightarrow \eta n p$ model is a promising option. Using this model, in this work, we study $\gamma d \rightarrow \eta n p$ at the ELPH kinematics, and examine the sensitivity of the ELPH experiment to $a_{\eta N}$.

In Fig. 7(left,top), differential cross sections for $\gamma d \rightarrow \eta n p$ at the ELPH kinematics is shown as a function of the η -neutron invariant mass ($M_{\eta n}$). While the impulse mechanism is dominant, the $\eta n \rightarrow \eta n$ FSI mechanism gives a sizable effect on the cross section: -40 to $+20\%$. On the other hand, as we expected for the ELPH kinematics, the other FSI mechanisms are well suppressed. The $\pi n \rightarrow \eta n$ FSI, for which we have data and thus control well, can change the cross sections by $\lesssim 9\%$, and the NN rescattering effect is very small for $M_{\eta n} \lesssim 1.5$ GeV. The result indicates that the

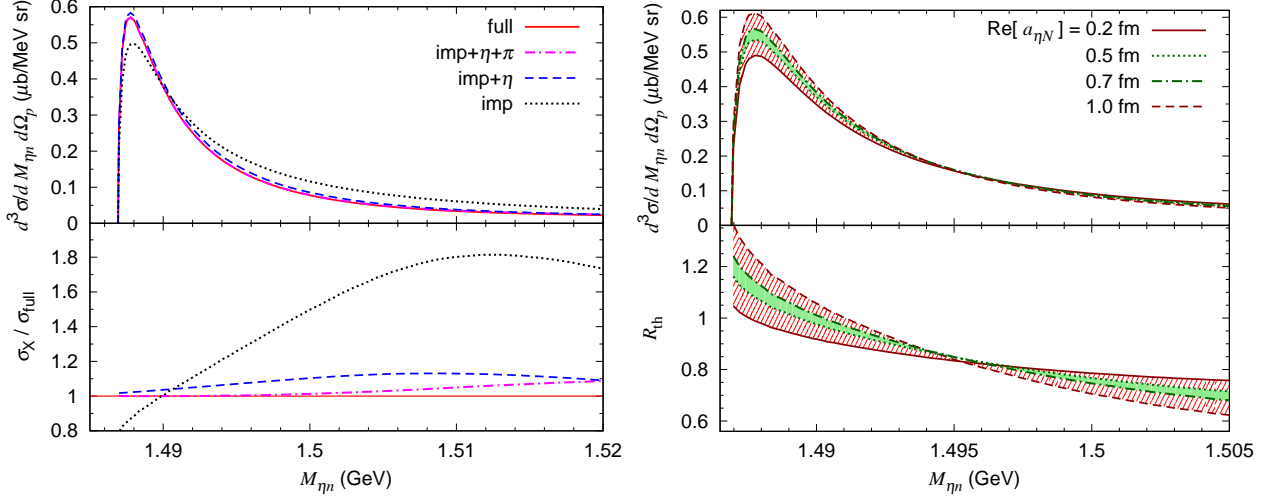


FIGURE 7. (Left,Top) Differential cross section for $\gamma d \rightarrow \eta p n$ at $E_\gamma = 0.94$ GeV and $\theta_p = 0^\circ$. The solid curve is from the full calculation while the dotted curve includes the impulse mechanism only. The dashed curve includes the impulse and η -exchange mechanisms, and the dash-dotted curve additionally includes the pion-exchange. The dash-dotted curve overlaps almost exactly with the solid curve. (Left,Bottom) The differential cross sections calculated with the various mechanisms divided by the full calculation. (Right,Top) $\text{Re}[a_{\eta N}]$ -dependence of $\gamma d \rightarrow \eta p n$ differential cross sections at $E_\gamma = 0.94$ GeV and $\theta_p = 0^\circ$. The curves are obtained with the full model by varying $\text{Re}[a_{\eta N}] = 0.2, 0.5, 0.7,$ and 1.0 fm; $\text{Im}[a_{\eta N}] = 0.25$ fm and $r_{\eta N} = 0$. (Right,Bottom) The ratio R_{th} of Eq. (1) for various values of $\text{Re}[a_{\eta N}]$. Figures taken from Ref. [18]. Copyright (2017) APS.

proton is well isolated from the ηn system, and thus we can safely neglect multiple rescatterings beyond the first-order rescattering.

Having shown that $\gamma d \rightarrow \eta p n$ cross sections at the ELPH kinematics are largely influenced by the $\eta n \rightarrow \eta n$ FSI, the next question is how sensitive the ELPH data is to $a_{\eta N}$. To address this question, in the $\gamma d \rightarrow \eta p n$ model, we replace the DCC $\eta n \rightarrow \eta n$ amplitudes with those of the effective range expansion. We then vary $a_{\eta N}$ and $r_{\eta N}$ (effective range) to examine how sensitively the $\gamma d \rightarrow \eta p n$ cross sections change. The result is shown in Fig. 7(right,top) where $\text{Re}[a_{\eta N}]$ is varied. The obtained cross sections are mostly within the red striped region. The change of the cross sections is more clearly seen in Fig. 7(right,bottom) showing the ratio defined by

$$R_{\text{th}}(M_{\eta n}) = \frac{d^3 \sigma_{\text{full}} / dM_{\eta n} d\Omega_p |_{\theta_p=0^\circ}}{d^3 \sigma_{\text{imp}} / dM_{\eta n} d\Omega_p |_{\theta_p=0^\circ}}, \quad (1)$$

where σ_{full} (σ_{imp}) is the cross section from the full model (impulse approximation). Because the ELPH are measuring both the proton and deuteron target data, and thus the experimental counterpart to R_{th} will be available. As shown in the figures, R_{th} changes by $\sim 25\%$ within the red striped region at $M_{\eta n} \sim 1.488$ GeV of the quasi-free (QF) peak. When $\text{Re}[a_{\eta N}]$ is varied by ± 0.1 fm from 0.6 fm, meanwhile, the cross sections change by $\sim 5\%$ at the QF peak as shown by the green solid bands. This indicates that R_{expt} data of 5% error per MeV bin can determine $\text{Re}[a_{\eta N}]$ at the precision of $\sim \pm 0.1$ fm. This is a significant improvement over the current uncertainty. The ELPH experiment is capable of achieving this precision measurement.

FSI corrections to neutrino-nucleon cross section data from neutrino-deuteron experiments

A reliable neutrino-nucleon reaction model is a key ingredient in developing a neutrino-nucleus reaction model to be used in neutrino-oscillation analyses. Regarding the single pion productions ($\nu N \rightarrow l\pi N$), many microscopic models with different dynamical contents have been developed. An overview of these microscopic models can be found in Ref. [27], and a detailed comparison in Ref. [28]. We stress that the total cross section data [9, 10] of $\nu_\mu p \rightarrow \mu^- \pi^+ p$, $\nu_\mu n \rightarrow \mu^- \pi^+ n$, and $\nu_\mu n \rightarrow \mu^- \pi^0 p$ play a crucial role in developing these models. All the models include the axial $\Delta(1232)$ -excitation mechanism, and the strength of this dominant piece is always fitted to the total

cross section data. However, the total cross section data currently available were actually extracted from neutrino-deuteron reaction ($\nu_\mu d \rightarrow \mu^- \pi NN$) data under an assumption that the quasifree mechanism dominates and FSI are negligible. Considering the precision needed for neutrino-nucleus reaction models in near-future neutrino oscillation analyses, we can no longer ignore the possible FSI effects, and thus we address this problem.

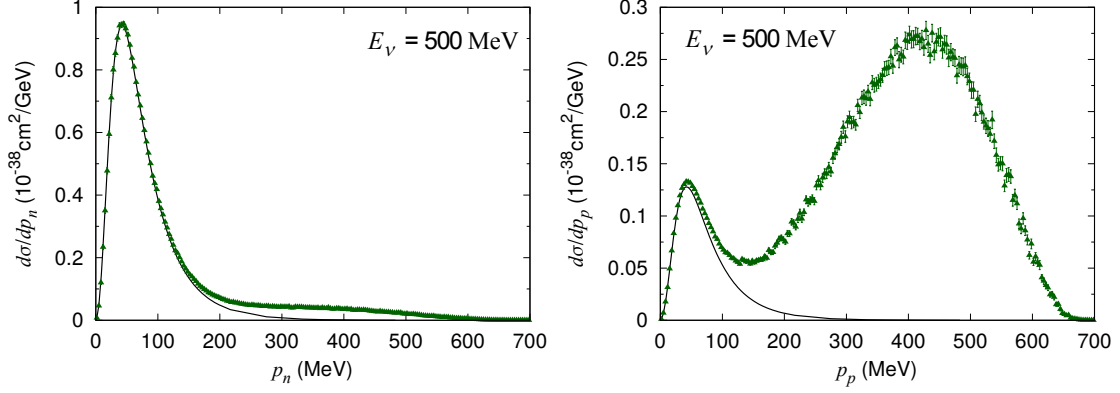


FIGURE 8. Neutron (left) and proton (right) momentum distributions in $\nu_\mu d \rightarrow \mu^- \pi^+ pn$ at $E_\nu = 0.5$ GeV. The impulse mechanism gives the green triangles. The black solid curve in the left (right) panel is obtained by convoluting the $\nu_\mu p \rightarrow \mu^- \pi^+ p$ ($\nu_\mu n \rightarrow \mu^- \pi^+ n$) cross sections with the deuteron wave function as in Eq. (2). The error bars are statistical from using the Monte-Carlo method for the phase-space integral.

We analyze the spectator momentum (p_s) distribution in $\nu_\mu d \rightarrow \mu^- \pi N' N_s$ (N_s : spectator). The p_s -distribution is a minimal information to extract the cross section for $\nu_\mu p \rightarrow \mu^- \pi^+ p$ ($\nu_\mu n \rightarrow \mu^- \pi^+ n$). This is because the quasifree neutrino-proton (neutrino-neutron) pion production process is expected to dominate exclusively in a low- p_n (p_p) region. This can be seen in Fig. 8 where we show the neutron and proton momentum distributions calculated with the impulse approximation, along with the $\nu_\mu N \rightarrow \mu^- \pi N'$ ($\equiv \alpha$) cross section convoluted with the deuteron wave function (Ψ_d):

$$\frac{d\tilde{\sigma}_\alpha(E_\nu)}{dp_s} = p_s^2 \int d\Omega_{p_s} \sigma_\alpha(\tilde{E}_\nu) |\Psi_d(\vec{p}_s)|^2, \quad (2)$$

where the total cross section σ_α is calculated with the same $\nu_\mu N \rightarrow \mu^- \pi N'$ amplitudes implemented in the $\nu_\mu d \rightarrow \mu^- \pi NN$ model; \tilde{E}_ν is the boosted neutrino energy. As p_s increases, the convoluted cross sections undershoot the impulse calculation because the other nucleon's contribution becomes more significant. This is more evident in the p_p -distribution in Fig. 8(right) because the cross section of $\nu_\mu p \rightarrow \mu^- \pi^+ p$ is ~ 9 times larger than that of $\nu_\mu n \rightarrow \mu^- \pi^+ n$ at this neutrino energy.

Now we examine the FSI effects in Fig. 9. The p_s -distribution ($d\sigma_{\nu_\mu d}/dp_s$) for $\nu_\mu d \rightarrow \mu^- \pi^+ pn$ is reduced significantly by the NN FSI as seen in the differences between the blue diamonds and green triangles in the figures. In particular, the quasifree peak in the low- p_s region is significantly lowered.

The significant FSI effects found above points to the necessity of correcting the deuterium bubble chamber data for the $\nu_\mu N \rightarrow \mu^- \pi N$ total cross sections [9, 10]. Using the FSI effects shown in Fig. 9, we correct the data and show them in Fig. 10 along with the original ones [30] for comparison. The correction enhances the cross sections by factors of 1.05–1.12, 1.10–1.27, and 1.01–1.02 for $\nu_\mu p \rightarrow \mu^- \pi^+ p$, $\nu_\mu n \rightarrow \mu^- \pi^+ n$, and $\nu_\mu n \rightarrow \mu^- \pi^0 p$, respectively. The correction is larger for smaller E_ν .

Summary

I reviewed our recent activity with the DCC approach. I discussed the DCC approach to the single nucleon sector such as the DCC analysis of $\pi N, \gamma N \rightarrow \pi N, \pi\pi N, \eta N, K\Lambda, K\Sigma$ reactions, and its extension to finite Q^2 region and neutrino-induced meson productions. Then I discussed applications of the DCC model amplitudes to electroweak meson productions on the deuteron: (i) the extraction of neutron-target observables from $\gamma d \rightarrow \pi NN$; (ii) a novel method of extracting η -nucleon scattering length from $\gamma d \rightarrow \eta np$; (iii) FSI corrections to neutrino-nucleon cross

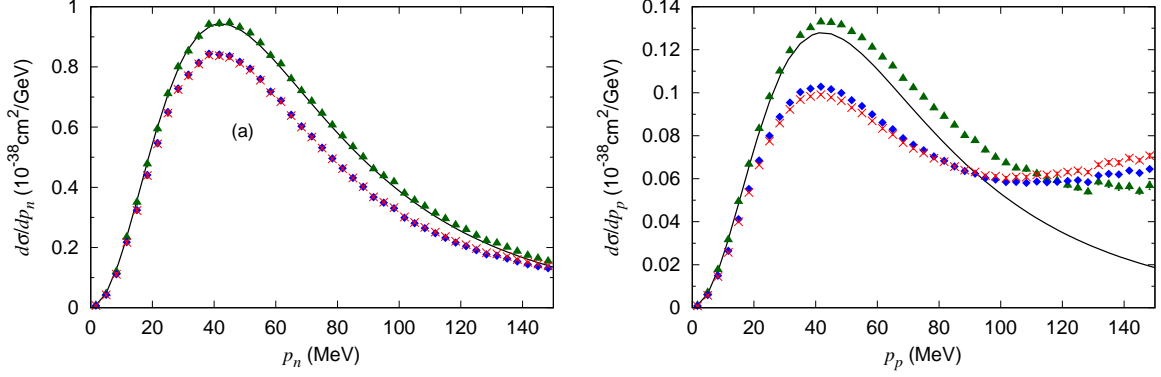


FIGURE 9. Neutron (left) and proton (right) momentum distributions in $\nu_\mu d \rightarrow \mu^- \pi^+ pn$ at $E_\nu = 0.5$ GeV. The impulse mechanism gives the green triangles, while the NN rescattering mechanism is also included in the blue diamonds. The red crosses are calculated with the full model including the impulse + NN + πN rescattering mechanisms. The $\nu_\mu p \rightarrow \mu^- \pi^+ p$ and $\nu_\mu n \rightarrow \mu^- \pi^+ n$ cross sections are convoluted with the deuteron wave function to give the black solid curves in the left and right panels, respectively. Figures taken from Ref. [29]. Copyright (2019) APS.

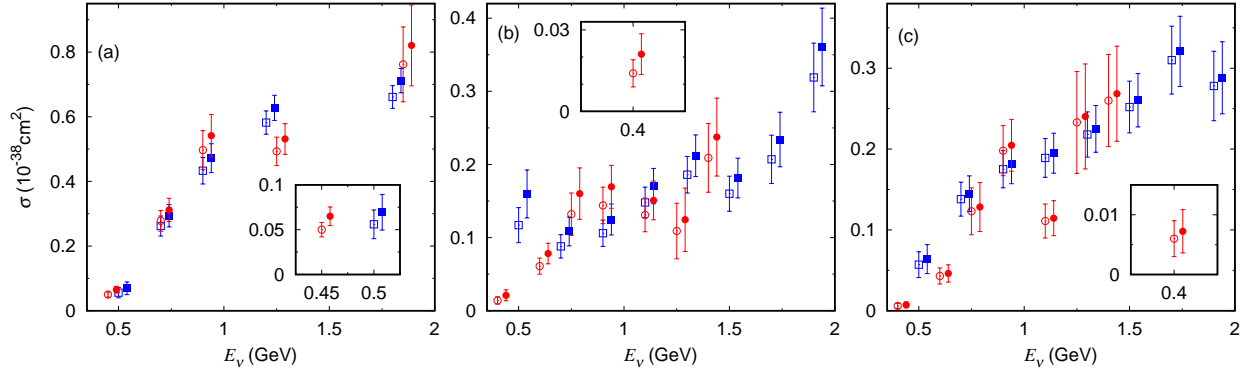


FIGURE 10. Total cross sections for (a) $\nu_\mu p \rightarrow \mu^- \pi^+ p$, (b) $\nu_\mu n \rightarrow \mu^- \pi^+ n$, and (c) $\nu_\mu n \rightarrow \mu^- \pi^0 p$. The open red circles and open blue squares are the reanalyzed ANL and BNL data [30], respectively, without applying cuts on W . The ANL and BNL data are corrected for the Fermi motion and FSI and shown by the solid red circles and solid blue squares, respectively. The inset shows an enlargement of the small E_ν region. Figures taken from Ref. [29]. Copyright (2019) APS.

section data from neutrino-deuteron experiments. Although not covered during the presentation because of the time limitation, I mention that the DCC approach has also been applied to analyzing $\bar{K}N$ reactions to extract hyperon resonance properties [31, 32, 33], and to describing FSI in heavy meson decays into three mesons [34, 35, 36].

ACKNOWLEDGMENTS

The author thanks H. Kamano, T.-S.H. Lee, T. Sato, and T. Ishikawa for collaborations on the subjects discussed in this manuscript. This work is in part supported by National Natural Science Foundation of China (NSFC) under contracts 11625523.

REFERENCES

- [1] H. Kamano, T.-S. H. Lee, S.X. Nakamura, and T. Sato, <http://www.phy.anl.gov/theory/research/anl-osaka-pwa/>
- [2] A.V. Anisovich, R. Beck, E. Klempt, V.A. Nikonov, A.V. Sarantsev, and U. Thoma, *Eur. Phys. J. A* **48**,15 (2012).

- [3] H. Kamano, S. X. Nakamura, T.-S. H. Lee, and T. Sato, Phys. Rev. C **88**, 035209 (2013).
- [4] H. Kamano, S.X. Nakamura, T.-S.H. Lee, and T. Sato, Phys. Rev. C **94**, 015201 (2016).
- [5] <http://t2k-experiment.org>
- [6] <http://www.dunescience.org>
- [7] Preliminary results from JLab E00-002, C. Keppel, M.I. Niculescu, spokespersons. Data files can be obtained at <https://hallcweb.jlab.org/resdata/database>.
- [8] S.X. Nakamura, H. Kamano, and T. Sato, Phys. Rev. D **92**, 074024 (2015).
- [9] S. J. Barish et al., Phys. Rev. D **19**, 2521 (1979).
- [10] T. Kitagaki et al., Phys. Rev. D **34**, 2554 (1986).
- [11] D. Day et al., Phys. Rev. D **28**, 2714 (1983).
- [12] R. Machleidt, Phys. Rev. C **63**, 024001 (2001).
- [13] B. Krusche et al., Eur. Phys. J. A **6**, 309 (1999).
- [14] U. Siodlaczek et al., Eur. Phys. J. A **10**, 365 (2001).
- [15] P. Benz et al. (Aachen-Bonn-Hamburg-Heidelberg-Muenchen Collaboration), Nucl. Phys. B **65**, 158 (1973).
- [16] B. Krusche et al., Phys. Lett. B **358**, 40 (1995).
- [17] S.X. Nakamura, H. Kamano, T.-S.H. Lee, and T. Sato, arXiv:1804.04757.
- [18] S.X. Nakamura, H. Kamano, and T. Ishikawa, Phys. Rev. C **96**, 042201(R) (2017).
- [19] S.X. Nakamura, Phys. Rev. C **98**, 042201(R) (2018).
- [20] W.J. Briscoe, A.E. Kudryavtsev, P. Pedroni, I.I. Strakovsky, V.E. Tarasov, and R.L. Workman, Phys. Rev. C **86**, 065207 (2012).
- [21] D. Ho et al. (CLAS Collaboration), Phys. Rev. Lett. **118**, 242002 (2017).
- [22] P.T. Mattione et al. (CLAS Collaboration), Phys. Rev. C **96**, 035204 (2017).
- [23] M. Dieterle et al. (A2 Collaboration), Phys. Rev. Lett. **112**, 142001 (2014).
- [24] M. Dieterle et al. (A2 Collaboration), Phys. Rev. C **97**, 065205 (2018).
- [25] Q. Haider and L. C. Liu, Int. J. Mod. Phys. E **24**, 1530009 (2015).
- [26] T. Ishikawa *et al.*, JPS Conf. Proc. **13**, 020031 (2017).
- [27] S.X. Nakamura, H. Kamano, Y. Hayato, M. Hirai, W. Horiuchi, S. Kumano, T. Murata, K. Saito, M. Sakuda, T. Sato, and Y. Suzuki, Rep. Prog. Phys. **80**, 056301 (2017).
- [28] J.E. Sobczyk, E. Hernández, S.X. Nakamura, J. Nieves, and T. Sato, Phys. Rev. D **98**, 073001 (2018).
- [29] S.X. Nakamura, H. Kamano, and T. Sato, Phys. Rev. D **99**, 031301(R) (2019).
- [30] P. Rodrigues, C. Wilkinson, and K. McFarland, Eur. Phys. J. C **76**, 474 (2016).
- [31] H. Kamano, S.X. Nakamura, T.-S.H. Lee, and T. Sato, Phys. Rev. C **90**, 065204 (2014).
- [32] H. Kamano, S.X. Nakamura, T.-S.H. Lee, and T. Sato, Phys. Rev. C **92**, 025205 (2015).
- [33] H. Kamano and T.-S.H. Lee, Phys. Rev. C **94**, 065205 (2016).
- [34] H. Kamano, S.X. Nakamura, T.-S.H. Lee, and T. Sato, Phys. Rev. D **84**, 114019 (2011).
- [35] S.X. Nakamura, H. Kamano, T.-S.H. Lee, and T. Sato, Phys. Rev. D **86**, 114012 (2012).
- [36] S.X. Nakamura, Phys. Rev. D **93**, 014005 (2016).